Title

Effects of surface diffusion in electrocatalytic CO2 reduction on Cu revealed by kinetic Monte Carlo simulations

Journal

The Journal of Chemical Physics, 155(16)

ISSN

0021-9606

Authors

Li, Jinghan
Maresi, Ilaria
Lum, Yanwei
et al.

Publication Date

2021-10-28

DOI

10.1063/5.0068517

Peer reviewed

Effects of Surface Diffusion in Electrocatalytic CO_2 Reduction on Cu Revealed by Kinetic Monte Carlo Simulations

Jinghan Li,[1,2,3] Ilaria Maresi,[4] Yanwei Lum,[5,6] and Joel W. Ager[2,3]

[1)]*State Key Laboratory of Metal Matrix Composites, School of Materials Science and Engineering, Shanghai Jiao Tong University, Shanghai 200240, China.*

[2)]*Joint Center for Artificial Photosynthesis, Materials Sciences Division, Lawrence Berkeley National Laboratory, Berkeley, CA 94720, USA.*

[3)]*Department of Materials Science and Engineering, University of California Berkeley, Berkeley, CA 94720, USA*

[4)]*Fung Institute, University of California Berkeley, Berkeley, CA 94720, USA*

[5)]*Institute of Materials Research and Engineering, Agency for Science, Technology and Research (A*STAR), 138632, Singapore*

[6)]*Department of Chemical and Biomolecular Engineering, National University of Singapore, 117585, Singapore*

(*Electronic mail: jwager@lbl.gov)

(Dated: 5 October 2021)

Kinetic Monte Carlo (KMC) methods are frequently used for mechanistic studies of thermally driven heterogeneous catalysis systems but are underused for electrocatalysis. Here, we develop a lattice KMC approach for electrocatalytic CO_2 reduction. The work is motivated by a prior experimental report which performed electroreduction of a mixed feed of $^{12}CO_2$ and ^{13}CO on Cu; differences in the ^{13}C content of C2 products ethylene and ethanol ($\Delta^{13}C$) were interpreted as evidence of site selectivity. The lattice KMC model considers the effect of surface diffusion on this system. In the limit of infinitely fast diffusion (mean-field approximation), the key intermediates $^{12}CO*$ and $^{13}CO*$ would be well-mixed on the surface and no evidence of site selectivity could have been observed. Using a simple two-site model and adapting a previously reported microkinetic model, we assess the effects of diffusion on the relative isotope fractions in the products, using estimated surface diffusion rate of CO* from literature reports. We find that size of the active sites and the total surface adsorbate coverage can have a large influence on the values of $\Delta^{13}C$ which can be observed. $\Delta^{13}C$ is less sensitive to CO* diffusion rate as long as it is within the estimated range. We further offer possible methods to estimate surface distribution of intermediates and to predict intrinsic selectivity of active sites based on experimental observations. The work illustrates the importance of considering surface diffusion in the study of electrochemical CO_2 reduction to multi-carbon products. Our approach is entirely based on freely available open-source code, so will be readily adaptable to other electrocatalytic systems.

CONTENTS

I. INTRODUCTION

Electrocatalytic CO_2 reduction (CO_2R), if powered by renewable electricity, is a possible way to produce hydrogen-carbon-based chemicals and fuels without increasing anthropogenic carbon emissions.[1,2] In particular, multi-carbon products such as ethylene, ethanol, and propanol which can be produced when Cu is employed as an electrocatalyst are predicted to be economically desirable.[3] However, Cu is not selective as an electrocatalyst, and, typically, a mixture of C1-C3 hydrocarbons and oxygenates is produced.[4] While it would be clearly beneficial to improve the selectivity of Cu-based CO_2R catalysts, the reaction mechanism is complex as a result of the large number of elementary steps and intermediates.[5]

Substantial progress has been made towards elucidating the reaction mechanism by using density functional theory (DFT) to calculate the binding energies of adsorbed intermediates and the energy barriers of the elementary steps which connect them.[6–9] When combined with zero-dimensional microkinetic models (MKMs), it is possible to predict the partial current densities of typically observed products (CO, methane, ethylene, etc.) and compare them to experimental observations.[7,8,10–21] A possible shortcoming of this approach of combining *ab-initio* calculation with MKM is that typically only the activity of a single active site, e.g., the (100) plane of Cu, is predicted.

There is also ample evidence that nanostructuring the Cu surface, for example, by repeated oxidation-reduction cycling,[22–27] can steer selectivity to C2 products. Moreover, the catalysts used in high-current density (>1 A cm^{-2}) demonstrations of electrochemical CO_2 reduction are nanostructured catalysts.[28,29] The different binding sites on these types of nanostructured Cu vary widely in their binding energy for CO*, which is believed to be the key intermediate for the formation of all C2 products on Cu.[30] Indeed, it would be expected that these different sites might conceivably have different selectivities to specific C2 products, for example, hydrocarbons *vs.* oxygenates.

Recently, evidence for this supposition was provided by Lum and Ager.[31] In their study, reduction of mixed feeds of $^{12}CO_2$ and ^{13}CO was performed on both oriented surfaces of Cu ((111) and (100)) and nanostructured "oxide-derived" Cu (OD Cu). Under these conditions, surface adsorbed CO* has two formation pathways: two-electron reduction of $^{12}CO_2$ to form ^{12}CO* and direct adsorption of dissolved ^{13}CO to form ^{13}CO*. Observation of differences in the ^{13}C content of C2 products ethylene and ethanol ($\Delta^{13}C$), which was observed on the nanostructured Cu but not on

the oriented surfaces, was interpreted as evidence of the presence of product-selective sites.

The observation of product-selective sites would not have been possible if the surface diffusion of ^{12}CO* and ^{13}CO* were much faster than the dimerization rate; in this fast diffusion case the isotopes on the surface would be well mixed and all the active sites would produce C2 products with the same isotope fraction. Evidently, the surface diffusion rate, at least on the nanostructured Cu, is sufficiently slow compared to the dimerization rate such that differences in the ^{13}C content of C2 products can be observed. Therefore, the question naturally arises as to whether the surface diffusion of intermediates between the active sites in these catalysts, which would not be captured by a 0-D microkinetic model, might be important. Thus, the lattice KMC approach developed in this study is designed to study competition between surface diffusion and the reaction of intermediates in CO_2 reduction quantitatively.

There are surprisingly few prior studies of lattice KMC as applied to electrocatalysis. Koper introduced the approach in the 1990s, examining electrochemical CO stripping on Pt and Pt-Ru surfaces.[32,33] In this case, the mobile surface intermediates are CO* and OH*. Korzeniewski and Kardash examined CO phase formation on single-crystal Pt, again in the context of CO stripping.[34] Recently, Chun *et al.* used a combined DFT and KMC approach to study electrocatalytic denitrification on Pt(100), finding that the initial NO* coverage affected the probability of different pathways.[35] However, we know of no prior application of the KMC method to electrochemical CO_2 reduction.

Here, we develop a lattice KMC approach for electrochemical CO and CO_2 reduction. We begin by considering the case with no surface diffusion (no-mix), and then introduce a simple two-site model (A, B) in which the relative rates of $^{12}CO_2$ reduction to ^{12}CO* and ^{13}CO adsorption to ^{13}CO* (P_A, P_B) and the branching ratios to hydrocarbon (ethylene) and oxygenate (ethanol) (S_A, S_B) are adjustable parameters (Section II A). The reaction network is constructed based on the MKM model of Goodpaster *et al.*[11] We estimate the surface diffusion rate of CO* on Cu based on the NMR observations of CO* diffusion on Pt,[36] the binding energy of CO* on Cu and Pt,[13,30], and a scaling relationship between the binding energy and the diffusion barrier (Section II B).[37] By these methods we obtain a reasonable range of CO* diffusion rates based on the binding energies calculated for CO* on various sites on Cu nanoparticles.[30]

For the simulation engine, we have adapted the open-source software package Zacros developed by Stamatakis and Vlachos.[38,39] (Section II C). With our electrocatalysis-oriented adaptions, Zacros can simulate and visualize electrochemical processes like cyclic voltammograms (CV) with

multiple trajectories as we show by validating our approach by comparison with the CO stripping results of Koper.[32]

The maximum difference in ^{13}C content between ethylene and ethanol ($\Delta^{13}C$) occurs when no surface diffusion is allowed (no-mix limit), whereas this difference is zero in the limit of infinite diffusion coefficient (mean field approximation, as assumed in MKMs). The KMC simulations consider intermediate cases and show that $\Delta^{13}C$ largely depends on the size of the two regions (A, B) and the total surface occupancy (Section III). Interestingly, $\Delta^{13}C$ is less sensitive to the CO* surface diffusion rate within and between Regions A and B, as long as it is in the estimated range. The simulation results are further compared with experimental observations (Section IV A). Finally, we outline some future directions for the applications of KMC approaches to electrochemical CO_2 reduction (Section IV B). The workflows we employ are in the form of Jupyter notebooks, and the notebooks and representative simulation input and output files have been shared in a publicly accessible repository on GitHub to permit general use by the electrocatalysis community.

II. COMPUTATIONAL METHODS

A. Two-site model

1. No surface diffusion (no-mix limit)

We develop the two-site model by initially considering a case in which no diffusion of intermediates on the surface occurs. In the study of Lum and Ager,[31] an OD Cu electrocatalyst was co-fed with $^{12}CO_2$ and ^{13}CO such the products generated contained both ^{13}C and ^{12}C. It was experimentally determined that the ^{13}C fraction was higher in hydrocarbon products such as ethylene compared to oxygenates such as ethanol (**Figure S1**), especially at the more positive potentials which were employed (e.g. -0.56 V *vs.* RHE). This behavior can be captured by assuming that OD Cu has two different product-specific active sites (A and B), and that the one which favors the generation of ethylene (B) has a faster rate of ^{13}CO adsorption as compared to $^{12}CO_2$ reduction. Similarly, the active site which favors ethanol (A) should have a slower rate of ^{13}CO adsorption as compared to $^{12}CO_2$ reduction. With these assumptions, Site B will have a larger relative fraction of ^{13}CO* compared to Site A.

In this model, two parameters determine the ^{13}C fraction in the products: the relative probabilities for adsorption of ^{13}CO and reduction of $^{12}CO_2$ to form CO* and the subsequent probabilities

of hydrocarbon *vs.* oxygenate products formed by CO* dimerization. For each site, we denote the relative probability of forming ^{13}CO* *via* ^{13}CO adsorption as P_A and P_B and the branching ratios towards ethylene as S_A and S_B for Sites A and B, respectively. As a further simplification, we assume ethylene and ethanol are the only products and that $P_A + P_B = 1$ and $S_A + S_B = 1$.

In this case with no surface diffusion, the fraction of ^{13}C content in the products ethylene and ethanol can be analytically expressed:

$$^{13}\mathrm{C}_{\mathrm{ethylene}} = 2P_AS_A + 1 - P_A - S_A, \tag{1a}$$

$$^{13}\mathrm{C}_{\mathrm{ethanol}} = P_A + S_A - 2P_AS_A. \tag{1b}$$

Thus, the difference in the ^{13}C fraction (Δ^{13}C), which was experimental observable, is:

$$\Delta^{13}\mathrm{C} = {}^{13}\mathrm{C}_{\mathrm{ethylene}} - {}^{13}\mathrm{C}_{\mathrm{ethanol}} = 4P_AS_A + 1 - 2P_A - 2S_A = (2P_A - 1)(2S_A - 1). \tag{2}$$

If $P_A = 0.5$, meaning that each site has the same rate of direct ^{13}CO adsorption and two electron reduction of $^{12}CO_2$, no difference in isotope fraction in the products will be observed as the relative populations of ^{13}CO* and ^{12}CO* will be the same on each site. A similar null result is predicted if the sites are not selective for hydrocarbons *vs.* oxygenates ($S_A = 0.5$). On the other hand, we can consider a more extreme case in which Site A is very selective for $^{12}CO_2$ reduction ($S_A = 0.1$) and only produces ethanol ($S_A = 0$) while Site B is very selective for ^{13}CO adsorption ($S_B = 0.9$) and only produces ethylene ($S_B = 1$): in this case $\Delta^{13}\mathrm{C} = 0.8$, meaning that ethylene will be highly enriched in ^{13}C compared to ethanol.

2. Site geometry

Diffusion of CO* on the surface will reduce the value of Δ^{13}C compared to the predictions of Equation 2 because CO* formed on Site A can travel to Site B to be coupled to form C2 products on Site B and *vice versa*. To capture the isotope mixing meditated by surface diffusion, we implement the two-site model on the catalyst surface by assuming that each type of site occupies an area of L sites $\times$ L sites arranged in a checkerboard pattern as shown in Scheme 1. The $2L \times 2L$ region in the orange circle represents one repeating unit. All simulations are conducted on a 200 sites $\times$ 200 sites lattice with periodic boundary conditions.

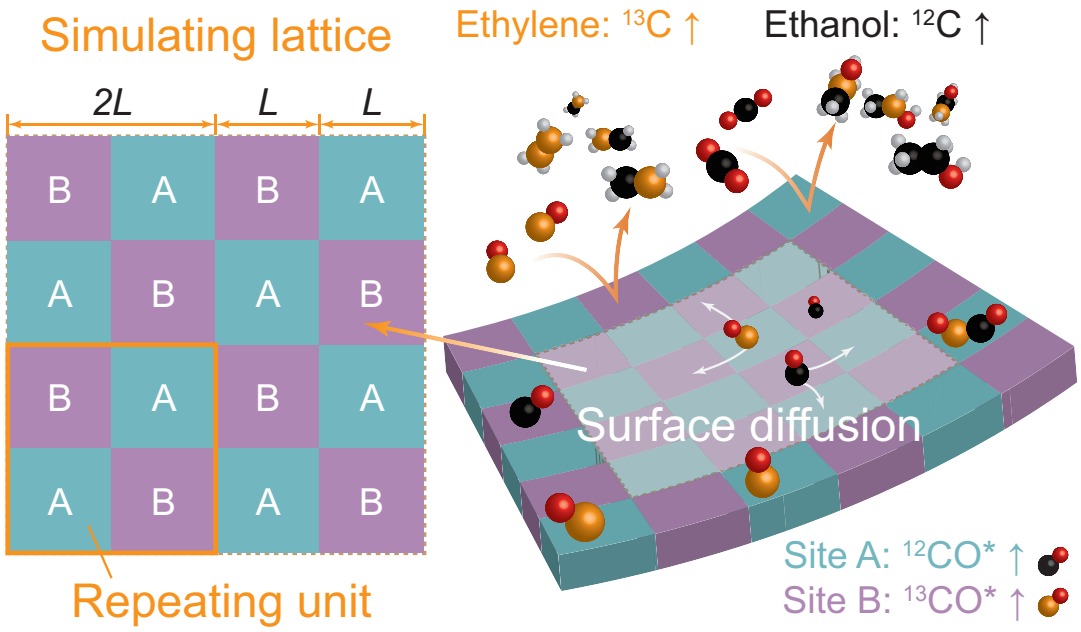

Scheme 1: Simulation design. A square lattice (200 sites × 200 sites) with periodic boundary conditions is used for the KMC simulations. Two types of active sites A and B are considered and the size of Region A or B is L sites × L sites, number of repeating units included is different for cases with different region size (L). The difference in ^{13}C content in the products ($\Delta^{13}C = {}^{13}C_{ethylene} - {}^{13}C_{ethanol}$) are compared for different conditions. For situations with both P_A and S_A smaller than 0.5 (smaller ^{13}CO* and lower selectivity to ethylene for Site A), $^{13}C_{ethylene}$ should be larger than $^{13}C_{ethanol}$ and $\Delta^{13}C$ should be > 0, which corresponds to the experimental observations.

3. Atomic lattice

There have been thorough investigations, both experimentally and theoretically, of the CO_2R activity and selectivity of the commonly exposed facets of Cu: (100), (110), and (111).[4,40] Here, we use Cu(100) for the atomic lattice as it has the highest selectivity for C2 products among the high-index surfaces of Cu. The lateral distance between the active sites for CO* adsorption for Cu(100) is $\frac{a}{\sqrt{2}}$, where a is the lattice constant of fcc copper ($a = 3.6$Å).[40] The impact of region size on ^{13}C content in the products was explored by varying L. A higher isotope mixing effect will be expected for a smaller region size (L), which corresponds to a shorter distance between the centers of Regions A and B.

B. Chemical network

1. Simplified reaction network

While more than 15 products can be generated during CO_2 reduction from Cu, including C1 to C3 products as well as byproducts H_2 from the competing reaction hydrogen evolution reaction (HER), we consider here a simplified pathway to C2 products *via* CO-CO coupling at adjacent atomic sites adapted from Goodpaster *et al.*[11] We note that the Goodpaster model has another pathway to C2 products *via* CO*+CHO* which is operative at higher overpotentials. Under the range of potentials considered in this work, -0.4 V to -0.8 V *vs.* RHE, we find that this competing pathway is slower than CO* dimerization (**Figure S2**) and thus do not include it in the model. With this simplification, the reaction network has four steps, with "*" and "**" denoting one and two adjacent empty surface sites, respectively.

$$\mathrm{CO(g)\ or\ CO_2(g)} + * \xrightarrow{k_1} \mathrm{CO^*} \tag{R1}$$

$$\mathrm{CO^* + CO^*} \underset{k_{-2}}{\overset{k_2}{\rightleftharpoons}} \mathrm{OCCO^{**}} \tag{R2}$$

$$\mathrm{OCCO^{**}} \xrightarrow{k_3} \mathrm{C_2H_4(g)\ or\ C_2H_5OH(g)} + ** \tag{R3}$$

$$\mathrm{CO^*} + * \xrightarrow{k_4} * + \mathrm{CO^*} \tag{R4}$$

R1 actually represents two elementary steps: the adsorption of ^{13}CO and the two-electron reduction of $^{12}CO_2$, which, if a mixed feed of CO and CO_2 is provided, will compete to form CO* on the surface. R2 describes the elementary step of CO-CO coupling, the shared reaction path for both C2 products. Further proton-coupled electron transfer steps towards ethylene (C_2H_4) and ethanol (C_2H_5OH) are represented by a lumped reaction (R3). Examples of possible detailed reaction pathways towards ethylene and ethanol that are lumped together here as R3 are provided in **Figure S3** in the **Supporting information (SI)**. Finally, R4 represents the surface diffusion of adsorbed CO*.

2. Rate constants

DFT simulations with an explicit solvent model suggest that the CO* coverage on Cu is around 0.3 at -0.5 V *vs.* RHE.[13] Therefore, we set the potential at -0.5 V *vs.* RHE at pH 7 for our

TABLE I: Rate constants for R1 required to maintain CO* coverage.[a]

Total coverage (θ)	0.3	0.5	0.7	0.9
H* coverage (θ_{H*})	0	0.2	0.4	0.6
k_1 (s^{-1})	2.754×10^{-3}	4.109×10^{-3}	7.487×10^{-3}	2.249×10^{-2}

[a] CO* coverage is 0.3 for all cases, while the total coverage is tuned by the amount of spectator H* added. For the values of k_1 shown in the table, the surface occupancy of CO* and thus the total coverage (θ) remain relatively stable during the simulation.

base case simulation. Simulations were initiated by placing ^{13}CO* and ^{12}CO* randomly on the surface. Specifically, the populations of ^{13}CO* and ^{12}CO* on Sites A and B were calculated using P_A, P_B, and θ, and the random seeding function of Zacros was used to distribute them on the respective sites. The impacts of total coverage on the surface diffusion of CO* were investigated by loading the surface with different amount of H*, which is a spectator in the chemical network. Other products, reactants like water, and other intermediates on the surface were not considered specifically, but the influence of these can be assessed by using the rate of R1 and the coverage of H* to tune the overall coverage. Table I summarizes the reaction rate constants (k_1) required to keep the CO* coverage constant at total surface coverage (θ) between 0.3 and 0.9.

The two branches of R1 are:

$$^{12}\mathrm{CO_2(g)} + * \xrightarrow{k_{1a}} {}^{12}\mathrm{CO}^* \tag{R1-1}$$

$$^{13}\mathrm{CO(g)} + * \xrightarrow{k_{1b}} {}^{13}\mathrm{CO}^* \tag{R1-2}$$

The rates for formation of ^{13}CO* and ^{12}CO* on Sites A and B are different and can be calculated based on P_A. Taking Site A as an example, to realize the branching ratio to ^{12}CO* (R1-1, P_B) and ^{13}CO* (R1-2, P_A), the rate constant k_{1a} and k_{1b} for ^{12}CO* and ^{13}CO*, respectively, should be in the following relationship, where $p = P_B/P_A$ is used for simplification. Details are in **SI** (**Table S1**).

$$\frac{k_{1a}}{k_{1b}} = \frac{P_B}{P_A} = p \longrightarrow k_{1a} = pk_{1b}, \tag{3a}$$

$$k_{1a} + k_{1b} = k_1 \longrightarrow (1+p)k_{1b} = k_1 \longrightarrow k_{1b} = k_1/(1+p). \tag{3b}$$

TABLE II: Rate constant parameters for R2 and R3.[a]

R2 forward (k_2)		R2 reverse (k_{-2})		R3 (k_3)	
a_2	b_2	a_{-2}	b_{-2}	a_3	b_3
-0.1723	0.4616	-0.3891	-0.0620	-0.1667	-0.1667

[a] Rate constants for R2 and R3 are given by Equation 4 with parameters summarized here.

CO-CO coupling (R2) is treated as reversible with k_2 and k_{-2} representing the forward and backward reactions, respectively. As shown in Equation 4, the reaction rates k_2 and k_{-2} are controlled by the free-energy barriers $G_i^\dagger$ which is a linear function of applied potential (V *vs.* SHE):

$$\Delta G_i^\dagger = a_i \times E + b_i, \tag{4a}$$

$$k_i = \frac{k_\mathrm{B}T}{h} \exp\left[-\Delta G_i^\dagger(E)/k_\mathrm{B}T\right] \tag{4b}$$

where k_B is Boltzmann's constant, h is Planck's constant, and values for a_i and b_i are given in Table II. Parameters in the rate constant format used by Zacros are shown in **Table S2**.

The proton-coupled electron transfers from the CO dimer towards ethylene and ethanol (R3) are also adapted from the Goodpaster model and are considered irreversible (Table II, Equation 4):

$$\mathrm{OCCO}^{**} \xrightarrow{k_{3a}} \mathrm{C_2H_4(g)} + ** \tag{R3-1}$$

$$\mathrm{OCCO}^{**} \xrightarrow{k_{3b}} \mathrm{C_2H_5OH(g)} + ** \tag{R3-2}$$

Taking Site A as an example, to realize the branching ratio to ethylene (R3-1, S_A) and ethanol (R3-2, S_B), the rate constants k_{3a} and k_{3b} for ethylene and ethanol, respectively, should be in the following relationship, with $s = S_A/S_B$ being used for simplification (**Table S3**).

$$\frac{k_{3a}}{k_{3b}} = \frac{S_A}{S_B} = s \longrightarrow k_{3a} = s\,k_{3b}, \tag{5a}$$

$$k_{3a} + k_{3b} = k_3 \longrightarrow (1+s)k_{3b} = k_3 \longrightarrow k_{3b} = k_3/(1+s). \tag{5b}$$

For OCCO** adsorbed across the boundary of Regions A and B, we assumed that the selectivity for ethylene and ethanol is the same ($S_{AB} = 0.5$).

TABLE III: Diffusion coefficient for CO* on Pt in electrolyte.[36]

θ_{CO} (CO* coverage)	1	0.68	0.46	0.36	0
D_{CO} (cm^2 s^{-1})	3.6×10^{-13}	8.1×10^{-13}	9.5×10^{-13}	1.5×10^{-12}	2.17×10^{-12}
Δ (nm s^{-1})[a]	12	18	19	24	29[b]

[a] The displacement per second is calculated from the formula: $\Delta = (4D_{\mathrm{CO}}t)^{1/2}$.

[b] This value is derived from the fitting curve of the displacement per second (Δ) *vs.* coverage (θ_{CO}).

3. Surface diffusion

Regarding R4, as far as we know, the CO* diffusion on the Cu surface has not been calculated or measured yet. However, measurements on other metals provide a basis for estimation. By applying ^{13}C electrochemical nuclear magnetic resonance (EC-NMR) to nanoparticle Pt catalysts, Babu *et al.* showed that the CO* diffuses on the surface at a rate of $\sim$10 nm s^{-1}.[36] As expected, the diffusion rate in electrolyte is much smaller than that in the gas and also decreases as the surface coverage of CO* increases. There is also a rule of thumb relating the barrier for diffusion to the binding energy, $E^* = -0.12BE - 0.02$ eV, where E^* is the diffusion barrier, and BE stands for the binding energy of the adsorbate in its most-stable site on the metal surface.[37] DFT simulations of the CO* BE with the same solvent environment have been conducted for both Cu and Pt;[13] these can be used to assess the difference in binding energies. Finally, a range of CO* binding energies Cu nanoparticles was reported in a combined DFT and machine learning study.[30]

Table III is reproduced from a previous report on CO* diffusion on Pt detected by EC-NMR, where the diffusion rate decreases as the surface coverage increases. We found out that the displacement of CO* per second (Δ in units of nm s^{-1}) is in linear relationship with the coverage, thus we fit Δ *vs.* θ_{CO} to predict the Δ value at 0 coverage, and further calculated the diffusion coefficient D_{CO} using the relationship $\Delta = (4D_{\mathrm{CO}}t)^{1/2}$. Assuming CO* diffuses on Pt by hopping between adjacent active sites with a density of 1.32×10^{15} sites cm^{-2},[32] the rate constant for Pt at 0 coverage is calculated to be 2864 s^{-1}.

Table IV provides the range of the binding energy for CO* on Cu with and without electrolyte obtained from the previous literature and compared to Pt. Specifically, the binding energy without electrolyte was extracted from the previous work showing the range of the binding energy of CO* on Cu nanoparticles, with Cu-High and Cu-Low representing the facets with highest and lowest

TABLE IV: Binding energy of CO* with Cu and Pt and the diffusion barrier derived from this.[13]

Facets	Binding energy without electrolyte (eV)	Estimated binding energy with electrolyte, BE (eV)	Diffusion barrier, E^* (eV)
Cu-High	−1.38	−0.85	0.0817
Cu(211), boundary	−1.06	−0.75	0.07
Cu(100)	−0.86	−0.62	0.0544
Cu(111)	−0.77	−0.48	0.0376
Cu-Low	−0.59	−0.24	0.0082
Pt		−1.62	0.1744

binding energy of CO* on Cu.[30] Another DFT calculation with explicit water model provides the value of CO* binding energy for commonly investigated facets of Cu and Pt including Cu(211), Cu(100), Cu(111), Pt(211), and Pt(111).[13] By comparing the binding energy with and without electrolyte, the range of binding energy of CO* on Cu in electrolyte conditions (BE for Cu-High and Cu-Low) are estimated with a fitting curve between binding energy with and without electrolyte for Cu(211), Cu(100), and Cu(111). We then use the average of BE for Pt(211) (−1.77 eV) and Pt(111) (−1.47 eV) to represent BE for Pt black (−1.62 eV) used in the NMR tests for surface diffusion rate, considering the surface of 10 nm Pt nanoparticle (similar to the Pt black (7 nm) in the EC-NMR test) contains various facets including {111} and other higher index facets, and small amount of {100} and {110}.[41] The diffusion barriers were then calculated from this using $E^* = -0.12BE - 0.02$ eV.[37]

Considering the two-site model, two scenarios should be considered for CO* diffusion, including k_4 representing the diffusion within Regions A and B, and k_{4AB} representing the diffusion across the boundary between Regions A and B. k_4 and the corresponding displacement per second of CO* were obtained based on the rate constant of Pt and the calculated ratio between Cu and Pt (Table V).

Specifically, the ratios among different facets are calculated by $e^{-\frac{E^*}{k_B T}}$, considering the CO* diffusion on Cu and Pt share the similar prefactor of 10^{13} s^{-1}. The calculated ratios were then used to derive the rate constants for CO* diffusion on Cu based on the rate for CO* diffusion on Pt with 0 CO* coverage (2864 s^{-1}). Assuming a Cu(100) surface with a distance between

TABLE V: Parameters for R4 within Regions A and B (k_4).

Facets	Cu-High	Cu(100)	Cu-Low
k_4 (s^{-1})	1×10^5	3×10^5	19×10^5
Δ^a (nm s^{-1})	161	279	703

[a] Displacement per second for near zero coverage.

TABLE VI: Parameters for R4 across the Regions A and B (k_{4AB}).

k_{4AB} (s^{-1})	5×10^4	1×10^5	2×10^5
Δ^a (nm s^{-1})	114	161	228

[a] Displacement per second for near zero coverage.

active sites of $\frac{a}{\sqrt{2}}$ (lattice constant $a = 3.6$Å), the displacement of CO* on Cu per second were calculated. As expected, because of its smaller binding energy, the diffusion rate for CO* on Cu is much larger compared with that on Pt, and we estimate that the displacement per second for near-zero coverage varies from 161 nm s^{-1} for facets with highest binding energy for CO* to 703 nm s^{-1} for facets with lowest binding energy with 279 nm s^{-1} for Cu(100) lying in between. We expect this estimated range of CO* diffusion rates on Cu is reasonable thus use it for the following simulations. We note that the effective surface diffusion distance of CO* on Cu will decrease with an increased surface coverage, and we will explore this effect in the simulations discussed in Section III B.

Regarding the diffusion rate across the boundary (k_{4AB}), Cu(211) composed of (111) terraces separated by (100) steps is one way to represent the boundaries between Regions A and B. Therefore, simulations with $k_{4AB} = 2 \times 10^5$ s^{-1} based on the binding energy (BE) of Cu(211) are used for base case in Section III C. We also considered the possibility that the boundary sites might have a larger binding energy than Cu(211), so simulations were also performed with smaller values of k_{4AB} as shown in Table VI.

C. KMC simulation methods

1. Simulation conditions

To ensure that steady state conditions could be captured, we simulated a very selective case with $S_A = P_A = 0.1$ for 360 s over a range of region sizes, total coverages, CO* binding energies, and boundary diffusion rates. In all cases, steady state behavior was reached within 180 s (**Figure S4**). As we expect less time to be required for less selective cases to reach steady state, all simulations described below were performed for 180 s. For each set of input parameters, simulations were run 10 times and the mean values are reported.

2. Adaptation of Zacros KMC code for electrocatalysis

Although the Zacros simulation platform we employed was developed for thermal catalysis,[42] it has a number of features that are well-suited to electrocatalysis, such as the equilibration of reversible steps, the use of a cluster Hamiltonian, and a scaling feature to speed up simulations if there are relatively fast or slow steps.[43] Moreover, the code developers have made available a number of Python wrapper scripts which prove to be very useful for simulation and data visualization.

However, electrocatalysis differs in some key aspects from thermal catalysis. Compared to thermal catalysis in which the absolute temperature can range within a relatively narrow range, the potentials which drive electrochemical reactions can be controlled in a very wide range, with small changes in potential on either side of the equilibrium condition producing extreme variations in the rate constants for elementary steps. As a result, turn-over frequency and selectivity in a given chemical network can depend sensitively on potential. Also, the changes in applied potential can be quite fast compared to the increase or decrease of the temperature in a thermally driven catalytic system.

Therefore, several adaptations for Zacros are required to enable application to heterogeneous electrocatalysis. As one example, as described in the **SI**, we used the generalized prefactor term in the Arrhenius expression to replicate Butler-Volmer behavior (Equation 4) with temperature serving as a proxy variable for potential. KMC simulations of CO stripping were conducted and compared with MKM predictions and KMC results from Koper.[32] Agreement was excellent as shown in **Figures S5-10**, validating the approach.

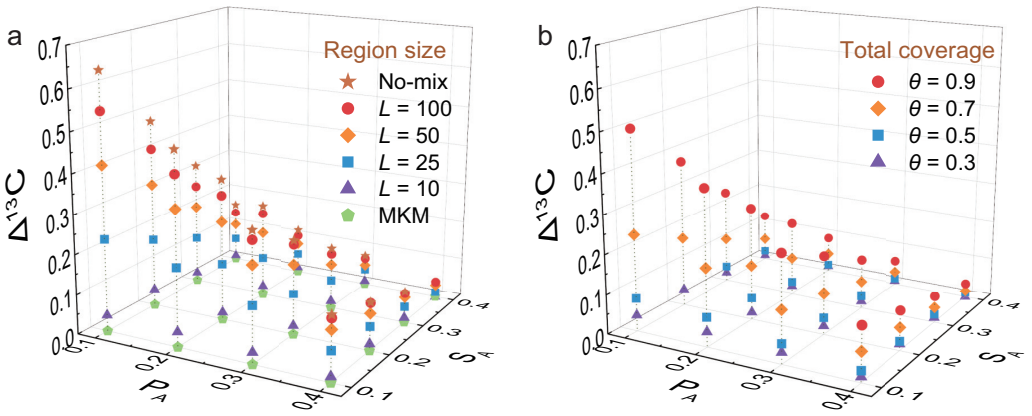

FIG. 1: Factors that have a large impact on Δ^{13}C. (a) KMC simulation results for active site sizes L between 10 and 100 sites compared with MKM prediction (Δ^{13}C = 0) and no-mixing limit, Equation 2. (b) KMC simulation results with various total surface coverages (θ) for active site size $L = 10$. Coverage of CO* is 0.3, $k_4 = 3 \times 10^5$ s^{-1}, and $k_{4AB} = 2 \times 10^5$ s^{-1} for all cases. Reported values are the average of 10 independent simulations. Numerical values are in **Tables S4 and S5**.

III. COMPUTATIONAL RESULTS

Referring back to Equation (2) which describes the no-mixing limit, if either P_A and S_A is smaller than 0.5, Δ^{13}C will be non-zero and, in principle, experimentally observable. Figure 1a shows the predictions of this model. For example, for $P_A = 0.1$, $S_A = 0.1$, Δ^{13}C = 0.64 (star in upper left corner of the 3D plot), while for a less selective case with $P_A = 0.4$, $S_A = 0.4$, the value is only 0.04 (star in lower right corner). In contrast, in the limit of the mean field approximation used in MKMs, Δ^{13}C is 0 for all conditions as shown by the green pentagons in Figure 1a, because the ^{12}CO* and ^{13}CO* on the surface will be completely mixed. We show in the following sections that cases with a finite diffusion rate for CO* on Cu lie in between these extremes, beginning with two factors which have a large influence on ^{13}C fraction in C2 products: the size of Region A, B (L sites per side) and the surface occupancy by adsorbates (θ).

A. Effect of region size

To assess the influence of active site size on Δ^{13}C, we varied L between 10 and 100, which corresponds to region sizes between 2.5 nm to 25.5 nm as shown in Table VII. Larger active site

TABLE VII: Region size L and the corresponding length

L (sites per side)	10	25	50	100
Length (nm)[a]	2.5	6.4	12.7	25.5

[a] The value is calculated based on Cu(100) lattice using the equation with a as the lattice constant of Cu: $\frac{a}{\sqrt{2}}L$.

areas have a longer average path length for CO* to diffuse to the other region, and we expect to have a larger Δ^{13}C value predicted for the same values of P_A and S_A compared to smaller active sites. This effect can be clearly seen in Figure 1a: in the $L = 100$ case, predicted values of Δ^{13}C are close to the no-mixing limit whereas for $L = 10$ they approach the mean-field approximation limit of zero. As a result, in the limit of small active sites which are less selective, it may not be possible to observe site selectivity by the isotope labelling approach. Conversely, for large (or well-separated) active sites, it will be possible to obtain evidence of site selectivity.

B. Effect of surface coverage

If CO* only travels by surface diffusion, we would expect that the distance it can travel before CO-CO coupling will depend on the surface coverage. Figure 1b shows that the total surface coverage can have a large influence on Δ^{13}C. Simulations were performed by fixing the coverage of CO* at 0.3 for all cases and tuning the total coverage by adding spectator H* on the surface. We fixed the active site size at $L = 10$ because very small values of Δ^{13}C are predicted at $\theta_{\mathrm{CO}} = 0.3$ in the absence of H* (purple triangles in both Figures 1a and 1b). With a small amount of H* added to the surface ($\theta = 0.5$, blue squares), the value of isotope difference only increases a little, suggested by the smaller distance between blue squares and purple triangles with the same active site properties (P_A and S_A, the same perpendicular line to the x-y plane in Figure 1b). Evidently, at smaller total coverage, CO* is still surrounded by a sufficient number of empty sites for diffusion to be effective in isotope scrambling.

However, when the total surface coverage is 0.7, the diffusion of CO* on the surface is substantially hindered, thus resulting in a large increase in Δ^{13}C. With further H* added until 0.9 of the surface is occupied (red circles), the increase in Δ^{13}C becomes even larger, suggesting with such a high surface occupancy, the diffusion of CO* on the surface towards the boundaries between different types of active sites before being transformed to the CO_2R products is much slower. In

this case, an observable difference in the ^{13}C fraction in C2 products might still be observable even though the active sites are quite close ($L = 10$, 2.5 nm).

C. Sensitivity to diffusion rate within Regions A and B (k_4)

As discussed before (Section II B 3), the possible range of surface diffusion rate of CO* on Cu is bounded by the range of the largest binding energy to the lowest binding energy of CO* on Cu. Therefore, here, we compared the impact of surface diffusion rate within this estimated range on the ^{13}C fraction in the products. Figure 2a summarizes the effect of diffusion rate within Regions A and B: cases considered use $k_4 = 1 \times 10^5,\ 3 \times 10^5$, and 19×10^5 s^{-1} corresponding to facets with highest binding energy (-0.85 eV), Cu(100) (-0.62 eV), and facets with lowest binding energy (-0.24 eV), respectively. Other parameters were region size $L = 25$, and diffusion rate across the boundary of Regions A and B $k_{4AB} = 2 \times 10^5$ s^{-1}. Surprisingly, Δ^{13}C is comparatively insensitive to the CO* diffusion rate compared to region size and surface occupancy, even with the large range of binding energies and the corresponding diffusion rates. Even for the case where the highest Δ^{13}C is expected ($P_A = S_A = 0.1$), the difference between the largest binding energy to the lowest are only 0.055. For the cases where the active sites are not so selective, the difference in Δ^{13}C is even smaller among facets with different binding energies.

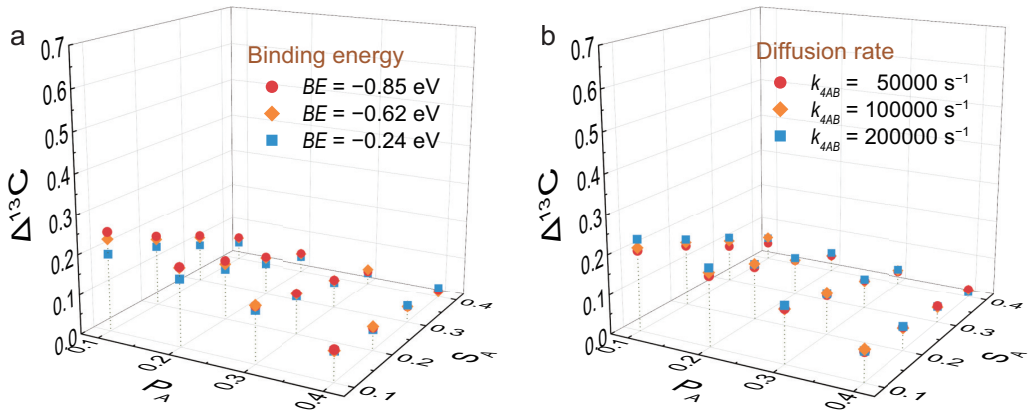

FIG. 2: Factors that have little impact on the isotope fraction in products. (a) Binding energy of CO* on Cu (*BE*) that influences the surface diffusion rate within Region A, B (k_4). Plots show the comparison for cases with -0.85, -0.62, -0.24 eV, representing the facets with highest CO* binding energy, Cu(100), and facets with lowest CO* binding energy. (b) Diffusion rate constant across the boundaries (k_{4AB}). $L = 25$ with a total coverage of 0.3 for all cases. The data in the plots are an average of 10 KMC trajectories, see tabulated values in **Tables S6 and S7**.

D. Sensitivity to diffusion rate across the boundary (k_{4AB})

We investigated the possibility that strong CO* binding at the boundaries between regions might slow the overall diffusion of CO*. For base case simulations we use the CO* diffusion rate on Cu(211) to represent the boundaries between Regions A and B ($k_{4AB} = 2 \times 10^5$ s^{-1}). Other situations with much higher binding energy, such as vacancies, can be envisioned to exist at the site boundaries. To capture their behavior, we decreased k_{4AB} to 1×10^5 and 5×10^4, s^{-1}, with these values corresponding to the largest CO* binding energy and half of it, respectively. Other parameters used were $L = 25$, and $k_4 = 3 \times 10^5$ s^{-1}. Similar to the effect of diffusion within the active site regions, the effect of diffusion rate across the boundary is small (Figure 2b). An additional effect might occur for very small active site areas. In this case, products generated at the boundaries will be a larger fraction of the total production. As we have assumed that the boundaries are not product selective, this would decrease the overall Δ^{13}C.

IV. DISCUSSION

A. Comparison with experimental observation

Our KMC simulations clearly show that surface diffusion of adsorbates reduces $\Delta^{13}C$ to a greater or lesser degree for all considered cases. As a result, measurement of $\Delta^{13}C$ with a mixed $^{13}CO/^{12}CO_2$ feed will provide an underestimate of the actual site selectivity. Furthermore, the sites need to be very selective in order for experimental evidence for them to be found in this way.

In the isotope labelling experiment, the difference in ^{13}C fraction in CO_2R products was only observed on OD Cu, but not on Cu(100) or Cu(111). The present results show that the null result for oriented Cu does not rule out the possibility that they may have product-selective sites, steps *vs.* terrace sites, for instance. Indeed, the impact of surface diffusion might be larger for oriented Cu compared to nanostructured OD Cu, because the latter may contain more defects that increase the CO* coverage or the coverage of spectator species, such that the overall diffusion rate is decreased, leading to a higher $\Delta^{13}C$ as depicted in Figure 1b.

The experimentally observed value for OD Cu was $\Delta^{13}C = 0.12$ at -0.56 V *vs.* RHE. We discuss here the selectivity and diffusion parameters which would allow this value to be observed. As we do not know the selectivities for ethylene *vs.* ethanol (S_A) and $^{12}CO_2$ reduction *vs.* ^{13}CO adsorption (P_A), these were varied parametrically for different active site areas ($L = 25,\ 50,\ 100$), total coverages ($\theta = 0.7,\ 0.9$), CO* binding energies (-0.24 eV, -0.62 eV, -0.85 eV), and k_{4AB} (5×10^4, 1×10^5, 1×10^5 s^{-1}), see **Figures S11-14** for details.

Figure 3a considers different region sizes (L). For all cases, either S_A or P_A needs to be smaller than 0.4 for $^{13}C = 0.12$, the experimentally observed value, to be predicted. For example, for $L = 25$, when the active sites are very product-selective ($S_A = 0.1$), P_A only needs to be 0.334, which is not very selective between CO_2 reduction and CO adsorption (P_A). However, when the sites are very similar and not obviously selective for specific product ($S_A = 0.3$), P_A needs to be 0.1, very selective for CO_2 reduction *vs.* CO adsorption. For the largest region size ($L = 100$) the requirements approach those of the no-mix limit, Equation 2. A clear shift to higher selectivity requirement is observed when the region size becomes smaller. For small region size ($L = 10$), no matter how selective the sites are (within the simulation range), the predicted $\Delta^{13}C$ is always less than 0.12. As a result, no parametric curve for this case is plotted. Figure 3b considers different total coverages (θ) for $L = 10$. For conditions with small total coverage (θ is 0.3 and 0.5), the

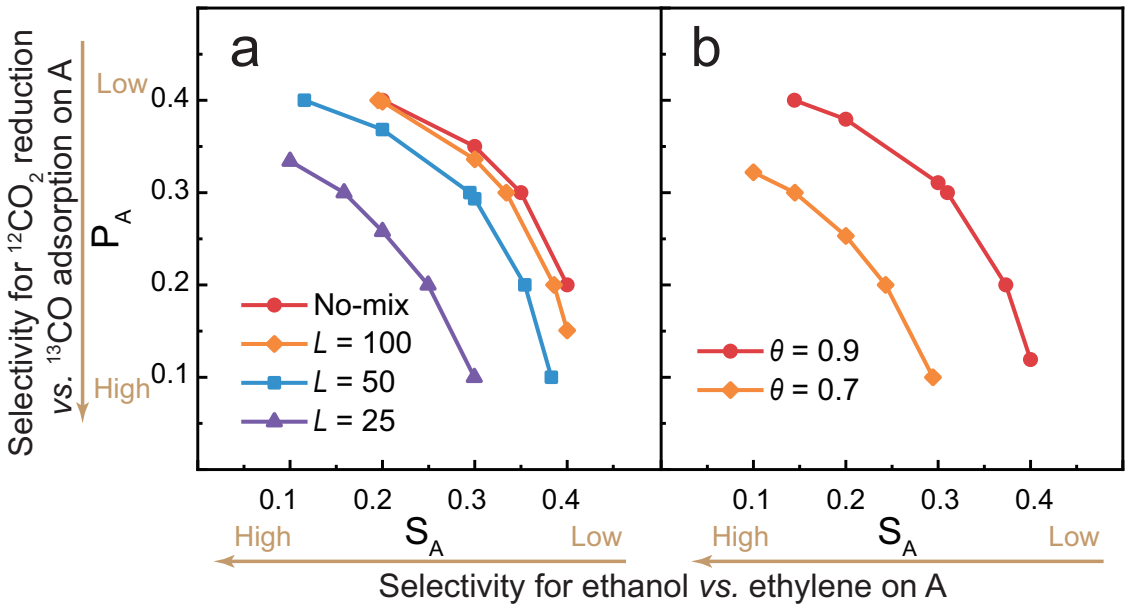

FIG. 3: Selectivity requirements (S_A and P_A) to observe $\Delta^{13}C = 0.12$. (a) Selectivity requirements for various active site sizes (L) and compared with no-mixing limit. (b) Selectivity requirements for various total surface coverage (θ) with active site size $L = 10$. Coverage of CO* is 0.3, $k_4 = 3 \times 10^5$ s^{-1}, and $k_{4AB} = 2 \times 10^5$ s^{-1} for all cases. Numerical values are in **Table S8**.

observed $\Delta^{13}C$ for all situations (S_A and P_A) is smaller than 0.12, thus not plotted. However, when the total surface occupancy increases (θ is 0.7 and 0.9), and the effective diffusion of CO* is limited, the isotope difference can be observed.

This analysis shows that relating the isotope labeling results to intrinsic site selectivity will require knowledge of the surface coverage of CO*. Moreover, controlled introduction of spectator species can be used to modulate the surface diffusion of CO* and thus quantify its influence. It is even conceivable that this approach could reveal site selectivity for oriented Cu. Finally, we evaluated the influence of diffusion within and between the sites but found, as could be expected by examination of Figure 2, that these have only a small influence on the selectivity requirements as expected (**Figure S15**).

We also note that $\Delta^{13}C$ observed from OD Cu decreases as the applied potential becomes more negative (**Figure S1**). With more negative potential applied, the surface occupancy should be higher although the composition may change,[13] and we could expect slower surface diffusion of CO* and hence a larger value of $\Delta^{13}C$, which is the opposite of the experimental observation. It appears that either the active sites become less selective for the generation of ethylene *vs.* ethanol

or less selective for CO_2 reduction *vs.* CO adsorption at more negative potentials. Another possibility might be that the more negative potential has triggered other less selective active sites, again reducing the value of $\Delta^{13}C$.

B. Limitations and possible extensions of KMC model

We have considered the simplest possible model that could yield the observed behavior. Here, we discuss limitations of the model and at same time provide some possible extensions which could be implemented if more information about the surface under electrocatalytic conditions were available.

In the present model, the domain size size L and the surface diffusion coefficient D_{CO} have a similar effect: i.e., decreasing L and/or increasing D_{CO} both lead to more isotopic mixing between the two regions. This naturally leads to the question as to why we considered them separately. Importantly, these two parameters have different physical origins and could, in principle, be controlled separately. For example, the oxidation/reduction cycling used to produce OD Cu is known to reduce the grain size (smaller L). At the same time, different facets and grain boundaries of Cu have different binding energies for CO. It is thus possible to imagine that KMC modelling of the type introduced here could be used to design catalysts which would balance these effects to control selectivity.

It is relevant to consider how the model could be extended to capture the complex interplay of the the gas/solid/liquid interface with the catalyst surface which is known to exist in electrochemical CO_2R.[4,28,44] Experimental information about the catalyst surface, including the active site size, the gas/adsorbate exchange rate, and surface diffusion would allow construction of models with fewer estimated parameters and conditions, hence yielding more useful insight.

We considered a very simple two-site model with $P_A + P_B = 1$ and $S_A + S_B = 1$, but CO_2 reduction on Cu can generate a variety of C1-C3 products. It would be straightforward to add pathways to additional products, particularly if the relevant intermediates and product ratios were known. Also, a more realistic surface model with inactive and/or non-selective sites could also be implemented. The boundaries between active regions could possess complete different properties from the active regions and may also have a gradual impact area that is not considered in the simplified two-site model. More types of active sites and specific designed lattice structures could be used to better describe the surface.

Our model only considered CO* transport by surface diffusion. However, there is some evidence that CO* can desorb and re-adsorb on the Cu surface during CO_2R.[45] In the context of an isotope labelling experiment, the ^{12}CO* reduced from the $^{12}CO_2$ may also have a chance to participate in the CO adsorption equilibrium and blend with the ^{13}CO feeding gas and be re-adsorbed to the surface. This scenario could be considered by adding a step describing the desorption of CO* based on the information of exchange rate ($CO* \rightleftharpoons CO(g)$) and the tracking of a near-surface reservoirs of CO(g).

In our two-site model, S_A and P_A are separately determined parameters. However, one might expect that, based on scaling relationships, that these descriptors would be correlated with each other. Thus, there is an opportunity to use DFT and/or molecular dynamics to narrows the range of values for S_A and P_A, particularly if the structure of the active sites is known.

The model only considered a single metal, Cu. The model could be extended to simulate bimetallic catalysts, where it has been proposed that CO* (CO) generated on CO-selective elements (Au, Ag) can spillover to Cu to be further reduced to multi-carbon products.[46–48] The KMC simulations could also track variations in surface occupancy, such as found in island formation of adsorbates.[49] Is is known that Cu can undergo non-uniform surface reconstruction during CO_2R; this can be captured by dynamically changing the lattice structure during the KMC simulations. Finally, the present model considers only C2 products. It could be extended to C3 products such as propanol, particularly if information on the surface diffusion of the C2 intermediates becomes known.

V. CONCLUSIONS

In summary, we have performed Kinetic Monte Carlo simulations of electrocatalytic CO_2 reduction on Cu, adopting the open source software Zacros to do so. We employed a two-site model (A, B) to investigate the impact of surface diffusion on the difference in ^{13}C fraction in C2 products ($\Delta^{13}C$) from electrocatalytic CO_2 reduction when Cu is cofed with ^{13}CO and $^{12}CO_2$. If Sites A and B have different selectivities for hydrocarbon vs. oxygenate production, differences in the ^{13}C content of these products would expected; however, fast surface diffusion would scramble the ^{13}CO* and ^{12}CO*, which would reduce the effect.

Results show that measurement of $\Delta^{13}C$ with a mixed $^{13}CO/^{13}CO_2$ feed will provide an underestimate of the actual site selectivity if the impact of surface diffusion is not considered. $\Delta^{13}C$ is

largely influenced by the active site size and the total surface occupancy, but is less sensitive to the diffusion rate within the region with identical active sites and across the boundaries between regions as long as it is in the estimated reasonable range for CO* on Cu based on previous research.

The comparison between KMC results and the experimental observations provide the requirements of site selectivity towards products and for CO_2 reduction *vs.* CO adsorption to observe the difference in ^{13}C fraction in products. If information on the surface coverage of CO or of its diffusion rate were available, the intrinsic selectivity of the active sites for C2 products could be determined. Finally, using the Python workflow with simple modifications, the presented KMC simulation approach can be easily adapted to other electrocatalytic systems.

SUPPLEMENTARY MATERIAL

The supplementary materials include: the experimental observation of the difference in isotope fraction observed on OD Cu and corresponding microkinetic model; the adaptations of Zacros for KMC simulations for electrochemical process; possible detailed reaction mechanisms; detailed parameter conversion process for two-site model; determination of simulation time and validation of the method by exhibiting the KMC simulation results for CO stripping; and supplementary simulation results.

AUTHOR CONTRIBUTIONS

JL, IM, and JWA conceptualized the study and JWA supervised the work. JL, IM, and JWA designed the simulation model and the reaction network. IM, JL, and JWA adapted the software Zacros with electrocatalytic features. JL and IM did the simulations. JL and JWA debugged code and developed the data visualization. YL and JWA provided constructive advice on data analysis and future directions. JL and JWA wrote the original draft of the manuscript and all authors contributed to its final editing.

CONFLICTS OF INTEREST

There are no conflicts to declare.

ACKNOWLEDGMENTS

This material is based upon work performed by the Joint Center for Artificial Photosynthesis, a DOE Energy Innovation Hub, supported through the Office of Science of the U.S.Department of Energy under Award No. DE-SC0004993. We thank Prof. Michail Stamatakis for advice on coding electrochemical rate constants and the Vlachos group for maintaining a repository of useful Python wrapper files for interfacing with Zacros. J.L. acknowledges financial support from the China Scholarship Council.

DATA AVAILABILITY STATEMENT

The data that support the findings of this study are openly available in [Electrocatalysis-with-Zacros] at `https://github.com/Euploea/Electrocatalysis-with-Zacros`.

REFERENCES

[1]J. M. Spurgeon and B. Kumar, "A comparative technoeconomic analysis of pathways for commercial electrochemical CO_2 reduction to liquid products," Energy Environ. Sci. **11**, 1536–1551 (2018).

[2]C. F. Shih, T. Zhang, J. Li, and C. Bai, "Powering the Future with Liquid Sunshine," Joule **2**, 1925–1949 (2018).

[3]O. S. Bushuyev, P. De Luna, C. T. Dinh, L. Tao, G. Saur, J. van de Lagemaat, S. O. Kelley, and E. H. Sargent, "What Should We Make with CO_2 and How Can We Make It?" Joule **2**, 825–832 (2018).

[4]S. Nitopi, E. Bertheussen, S. B. Scott, X. Liu, A. K. Engstfeld, S. Horch, B. Seger, I. E. L. Stephens, K. Chan, C. Hahn, J. K. Nørskov, T. F. Jaramillo, and I. Chorkendorff, "Progress and Perspectives of Electrochemical CO_2 Reduction on Copper in Aqueous Electrolyte," Chem. Rev. **119**, 7610–7672 (2019).

[5]A. A. Peterson, F. Abild-Pedersen, F. Studt, J. Rossmeisl, J. K. Nørskov, and J. K. Norskov, "How copper catalyzes the electroreduction of carbon dioxide into hydrocarbon fuels," Energy Environ. Sci. **3**, 1311 (2010).

[6]B. W. J. Chen, L. Xu, and M. Mavrikakis, "Computational Methods in Heterogeneous Catalysis," Chem. Rev. **121**, 1007–1048 (2021).

[7]T. Cheng, H. Xiao, and W. A. Goddard, "Reaction Mechanisms for the Electrochemical Reduction of CO_2 to CO and Formate on the Cu(100) Surface at 298 K from Quantum Mechanics Free Energy Calculations with Explicit Water," J. Am. Chem. Soc. **138**, 13802–13805 (2016).

[8]X. Liu, P. Schlexer, J. Xiao, Y. Ji, L. Wang, R. B. Sandberg, M. Tang, K. S. Brown, H. Peng, S. Ringe, C. Hahn, T. F. Jaramillo, J. K. Nørskov, and K. Chan, "pH effects on the electrochemical reduction of $CO(_2)$ towards C_2 products on stepped copper," Nat. Commun. **10**, 1–10 (2019).

[9]F. Calle-Vallejo, R. F. De Morais, F. Illas, D. Loffreda, and P. Sautet, "Affordable Estimation of Solvation Contributions to the Adsorption Energies of Oxygenates on Metal Nanoparticles," J. Phys. Chem. C **123**, 5578–5582 (2019).

[10]Y. Li, H. Su, S. H. Chan, and Q. Sun, "CO_2 Electroreduction Performance of Transition Metal Dimers Supported on Graphene: A Theoretical Study," ACS Catal. **5**, 6658–6664 (2015).

[11]J. D. Goodpaster, A. T. Bell, and M. Head-Gordon, "Identification of Possible Pathways for C-C Bond Formation during Electrochemical Reduction of CO_2: New Theoretical Insights from an Improved Electrochemical Model," J. Phys. Chem. Lett. **7**, 1471–1477 (2016).

[12]H. Xiao, T. Cheng, and W. A. Goddard, "Atomistic Mechanisms Underlying Selectivities in C_1 and C_2 Products from Electrochemical Reduction of CO on Cu(111)," J. Am. Chem. Soc. **139**, 130–136 (2017).

[13]X. Liu, J. Xiao, H. Peng, X. Hong, K. Chan, and J. K. Nørskov, "Understanding trends in electrochemical carbon dioxide reduction rates," Nat. Commun. **8**, 15438 (2017).

[14]M. R. Singh, J. D. Goodpaster, A. Z. Weber, M. Head-Gordon, and A. T. Bell, "Mechanistic insights into electrochemical reduction of CO_2 over Ag using density functional theory and transport models," Proc. Natl. Acad. Sci. U. S. A. **114**, E8812–E8821 (2017).

[15]H. Liu, J. Liu, and B. Yang, "Computational insights into the strain effect on the electrocatalytic reduction of CO_2 to CO on Pd surfaces," Phys. Chem. Chem. Phys. **22**, 9600–9606 (2020).

[16]H. Liu, J. Liu, and B. Yang, "Modeling the effect of surface CO coverage on the electrocatalytic reduction of CO_2 to CO on Pd surfaces," Phys. Chem. Chem. Phys. **21**, 9876–9882 (2019).

[17]Y. Feng, W. An, Z. Wang, Y. Wang, Y. Men, and Y. Du, "Electrochemical CO_2 Reduction Reaction on M@Cu(211) Bimetallic Single-Atom Surface Alloys: Mechanism, Kinetics, and Catalyst Screening," ACS Sustain. Chem. Eng. **8**, 210–222 (2020).

[18]L. D. Chen, M. Urushihara, K. Chan, and J. K. Nørskov, "Electric Field Effects in Electrochemical CO_2 Reduction," ACS Catal. **6**, 7133–7139 (2016).

[19]G. Zhu, Y. Li, H. Zhu, H. Su, S. H. Chan, and Q. Sun, "Curvature-Dependent Selectivity of CO_2 Electrocatalytic Reduction on Cobalt Porphyrin Nanotubes," ACS Catal. **6**, 6294–6301 (2016).

[20]B. Ren, J. Li, G. Wen, L. Ricardez-Sandoval, and E. Croiset, "First-Principles Based Microkinetic Modeling of CO_2 Reduction at the Ni/SDC Cathode of a Solid Oxide Electrolysis Cell," J. Phys. Chem. C **122**, 21151–21161 (2018).

[21]S. Q. Xiang, S. T. Gao, J. L. Shi, W. Zhang, and L. B. Zhao, "Developing micro-kinetic model for electrocatalytic reduction of carbon dioxide on copper electrode," J. Catal. **393**, 11–19 (2021).

[22]C. W. Li and M. W. Kanan, "CO_2 Reduction at Low Overpotential on Cu Electrodes Resulting from the Reduction of Thick Cu_2O Films," J. Am. Chem. Soc. **134**, 7231–7234 (2012).

[23]C. W. Li, J. Ciston, and M. W. Kanan, "Electroreduction of carbon monoxide to liquid fuel on oxide-derived nanocrystalline copper," Nature **508**, 504–507 (2014).

[24]R. Kas, R. Kortlever, A. Milbrat, M. T. M. Koper, G. Mul, and J. Baltrusaitis, "Electrochemical CO_2 reduction on Cu_2O-derived copper nanoparticles: controlling the catalytic selectivity of hydrocarbons," Phys. Chem. Chem. Phys. **16**, 12194 (2014).

[25]H. Mistry, A. S. A. S. Varela, C. S. C. S. C. S. Bonifacio, I. Zegkinoglou, I. Sinev, Y.-W. Y.-W. Choi, K. Kisslinger, E. A. E. A. Stach, J. C. J. C. Yang, P. Strasser, and B. R. B. R. B. R. Cuenya, "Highly selective plasma-activated copper catalysts for carbon dioxide reduction to ethylene," Nat. Commun. **7**, 12123 (2016).

[26]Y. Lum, B. Yue, P. Lobaccaro, A. T. Bell, and J. W. Ager, "Optimizing C–C Coupling on Oxide-Derived Copper Catalysts for Electrochemical CO_2 Reduction," J. Phys. Chem. C **121**, 14191–14203 (2017).

[27]J. E. Pander, D. Ren, Y. Huang, N. W. X. Loo, S. H. L. Hong, and B. S. Yeo, "Understanding the Heterogeneous Electrocatalytic Reduction of Carbon Dioxide on Oxide-Derived Catalysts," ChemElectroChem **5**, 219–237 (2018).

[28]C.-T. Dinh, T. Burdyny, M. G. Kibria, A. Seifitokaldani, C. M. Gabardo, F. P. García de Arquer, A. Kiani, J. P. Edwards, P. De Luna, O. S. Bushuyev, C. Zou, R. Quintero-Bermudez, Y. Pang, D. Sinton, and E. H. Sargent, "CO_2 electroreduction to ethylene via hydroxide-mediated copper catalysis at an abrupt interface," Science **360**, 783–787 (2018).

[29]F. P. García de Arquer, C. T. Dinh, A. Ozden, J. Wicks, C. McCallum, A. R. Kirmani, D. H. Nam, C. Gabardo, A. Seifitokaldani, X. Wang, Y. C. Li, F. Li, J. Edwards, L. J. Richter, S. J. Thorpe, D. Sinton, and E. H. Sargent, "CO_2 electrolysis to multicarbon products at activities

greater than 1 A cm^{-2}," Science **367**, 661–666 (2020).

[30]Y. Huang, Y. Chen, T. Cheng, L.-W. W. Wang, and W. A. Goddard, "Identification of the Selective Sites for Electrochemical Reduction of CO to C_{2+} Products on Copper Nanoparticles by Combining Reactive Force Fields, Density Functional Theory, and Machine Learning," ACS Energy Lett. **3**, 2983–2988 (2018).

[31]Y. Lum and J. W. Ager, "Evidence for product-specific active sites on oxide-derived Cu catalysts for electrochemical CO_2 reduction," Nat. Catal. **2**, 86–93 (2019).

[32]M. T. M. Koper, A. P. J. Jansen, R. A. Van Santen, J. J. Lukkien, and P. A. J. Hilbers, "Monte Carlo simulations of a simple model for the electrocatalytic CO oxidation on platinum," J. Chem. Phys. **109**, 6051–6062 (1998).

[33]M. T. M. Koper, J. J. Lukkien, A. P. J. Jansen, and R. A. van Santen, "Lattice Gas Model for CO Electrooxidation on Pt-Ru Bimetallic Surfaces," J. Phys. Chem. B **103**, 5522–5529 (1999).

[34]C. Korzeniewski and D. Kardash, "Use of a Dynamic Monte Carlo Simulation in the Study of Nucleation-and-Growth Models for CO Electrochemical Oxidation," J. Phys. Chem. B **105**, 8663–8671 (2001).

[35]H.-J. Chun, V. Apaja, A. Clayborne, K. Honkala, and J. Greeley, "Atomistic Insights into Nitrogen-Cycle Electrochemistry: A Combined DFT and Kinetic Monte Carlo Analysis of NO Electrochemical Reduction on Pt(100)," ACS Catal. **7**, 3869–3882 (2017).

[36]P. K. Babu, J. H. Chung, E. Oldfield, and A. Wieckowski, "CO surface diffusion on platinum fuel cell catalysts by electrochemical NMR," Electrochim. Acta **53**, 6672–6679 (2008).

[37]A. U. Nilekar, J. Greeley, and M. Mavrikakis, "A simple rule of thumb for diffusion on transition-metal surfaces," Angew. Chemie - Int. Ed. **45**, 7046–7049 (2006).

[38]M. Stamatakis and D. G. Vlachos, "A graph-theoretical kinetic Monte Carlo framework for on-lattice chemical kinetics," J. Chem. Phys. **134**, 214115 (2011).

[39]J. Nielsen, M. D'Avezac, J. Hetherington, and M. Stamatakis, "Parallel kinetic Monte Carlo simulation framework incorporating accurate models of adsorbate lateral interactions," J. Chem. Phys. **139** (2013), 10.1063/1.4840395.

[40]K. M. Gameel, I. M. Sharafeldin, A. U. Abourayya, A. H. Biby, and N. K. Allam, "Unveiling CO adsorption on Cu surfaces: New insights from molecular orbital principles," Phys. Chem. Chem. Phys. **20**, 25892–25900 (2018).

[41]T. Altantzis, I. Lobato, A. De Backer, A. Béché, Y. Zhang, S. Basak, M. Porcu, Q. Xu, A. Sánchez-Iglesias, L. M. Liz-Marzán, G. Van Tendeloo, S. Van Aert, and S. Bals, "Three-

Dimensional Quantification of the Facet Evolution of Pt Nanoparticles in a Variable Gaseous Environment," Nano Lett. **19**, 477–481 (2019).

[42]M. Stamatakis and D. G. Vlachos, "Unraveling the complexity of catalytic reactions via kinetic monte carlo simulation: Current status and frontiers," ACS Catal. **2**, 2648–2663 (2012).

[43]E. C. Dybeck, C. P. Plaisance, and M. Neurock, "Generalized Temporal Acceleration Scheme for Kinetic Monte Carlo Simulations of Surface Catalytic Processes by Scaling the Rates of Fast Reactions," J. Chem. Theory Comput. **13**, 1525–1538 (2017).

[44]T. Burdyny and W. A. Smith, "CO_2 reduction on gas-diffusion electrodes and why catalytic performance must be assessed at commercially-relevant conditions," Energy Environ. Sci. **12**, 1442–1453 (2019).

[45]A. Wuttig, C. Liu, Q. Peng, M. Yaguchi, C. H. Hendon, K. Motobayashi, S. Ye, M. Osawa, and Y. Surendranath, "Tracking a common surface-bound intermediate during CO_2-to-fuels catalysis," ACS Cent. Sci. **2**, 522–528 (2016).

[46]Y. Wang, D. Wang, C. J. Dares, S. L. Marquard, M. V. Sheridan, and T. J. Meyer, "CO_2 reduction to acetate in mixtures of ultrasmall $(Cu)_n$,$(Ag)_m$ bimetallic nanoparticles," Proceedings of the National Academy of Sciences **115**, 278–283 (2018).

[47]J. Huang, M. Mensi, E. Oveisi, V. Mantella, and R. Buonsanti, "Structural Sensitivities in Bimetallic Catalysts for Electrochemical CO_2 Reduction Revealed by Ag-Cu Nanodimers," J. Am. Chem. Soc. **141**, 2490–2499 (2019).

[48]L. R. L. Ting, O. Piqué, S. Y. Lim, M. Tanhaei, F. Calle-Vallejo, and B. S. Yeo, "Enhancing CO_2 Electroreduction to Ethanol on Copper-Silver Composites by Opening an Alternative Catalytic Pathway," ACS Catalysis **10**, 4059–4069 (2020).

[49]R. M. Ziff, E. Gulari, and Y. Barshad, "Kinetic Phase Transitions in an Irreversible Surface-Reaction Model," Physical Review Letters **56**, 2553–2556 (1986).